

Emergence of local ordering and giant number fluctuations in active turbulence

Kirti Kashyap,^{1,*} Kolluru Venkata Kiran,^{2,†} and Anupam Gupta^{1,‡}

¹Department of Physics, Indian Institute of Technology Hyderabad, Hyderabad, India

²Université Côte d'Azur, CNRS, Institut de Physique de Nice (INPHYNI), 17 rue Julien Lauprêtre, 06200 Nice, France

We study spatiotemporal chaos in dense active suspensions using a generalized hydrodynamic model. As the activity is increased, we observe a clear structural transition marked by the formation of intense, spatially organized vortices with the appearance of giant number fluctuations. This transition is accompanied by the emergence of local polar ordering, an increase in velocity correlations, and a shift in the velocity distribution from unimodal to bimodal. Beyond activity, reducing the instability timescale leads to similar structural changes in the flow. This suggests that both activity and instability dynamics can serve as control parameters for pattern formation. Our findings reveal how local ordering and dynamical instability interact to generate large-scale structures in active systems. Furthermore, based on the energy budget, we define an order parameter that quantifies the structural changes in the phase space of activity and instability time scales.

Introduction: The collective behavior of active particles gives rise to complex and intriguing phenomena, including large-scale coherent motion in flocks, mesoscale turbulence in bacterial suspension, and defect-driven chaos in active liquid crystals [1–13]. The spatiotemporal structures observed in dense suspensions of active matter qualitatively resemble those found in passive turbulence systems [1, 8–10, 14–16]. Extensive studies have been conducted to investigate whether active turbulence shares similarities with or deviates from inertial turbulence. These investigations often focus on identifying universal features, such as power-law scaling and intermittency, which are hallmarks of turbulent systems [17–21]. Transitions in the flow characteristics are observed at critical values of the activity parameter, characterized by increased intermittency and deviations from Gaussian statistics [19, 22]. Until recently, there was no consensus on the existence of universal features in active turbulence. A recent study led by Ray [19] reported the emergence of universal scaling behavior in the energy spectrum beyond a critical activity threshold, highlighting the intricate interplay between active forcing and the system's underlying field dynamics.

However, there is also evidence pointing to structural changes in the vorticity field itself with increasing activity [23–27]. This highlights the need for a deeper understanding of how these emergent structures contribute to the observed universal and nonuniversal features of active turbulence. Gaining insight into these structural changes and flow dynamics is important for explaining various processes like nutrient mixing and molecular transport in biological and ecological systems. [15, 28–30].

In this work, we employ hydrodynamic models developed to describe the complex, chaotic flows in dense, quasi-two-dimensional bacterial suspensions [8, 19, 22]. These models have also been used to study turbulence-like behavior in dense suspensions of *Bacillus subtilis* [1, 21]. We focus on the emergence and evolution of spatiotemporal structural patterns as a

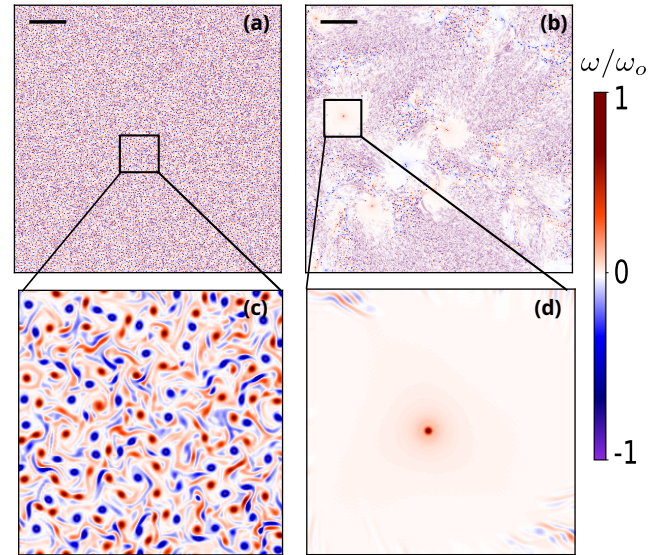


FIG. 1: The vorticity field (ω) is shown for two different activity levels: (a) $\alpha = -1$, and (b) $\alpha = -9$. The scale bar in both panels corresponds to 25Λ . Panels (c) and (d) present zoomed-in sections of the respective vorticity fields, with magnified regions chosen to be of the same order as the scale bar. The vorticity snapshot at higher activity displays spatial inhomogeneities, characterized by intense vortex regions coexisting with areas of negligible vorticity. The color bar is normalized by the maximum vorticity ω_0 of the respective α .

function of an activity parameter. Increasing activity leads to a strikingly uneven distribution of intense vorticity centers in space and time; see, for example, Fig 1. Tracking the number of vortex centers reveals the emergence of giant number fluctuations, hinting at an underlying structural transition in the flow. To probe the underlying origin of this transition, we examine the spatial velocity correlations and observe a marked increase in correlation length, along with the onset of local polar ordering. Interestingly, these locally ordered regions do not take over the whole system; instead, they coexist with disordered, chaotic zones. Similar structures have been observed experimentally [12]. Furthermore, we find that tuning the linear instability growth timescale—introduced to model the in-

* ph21resch11001@iith.ac.in

† kiran8147@gmail.com

‡ agupta@phy.iith.ac.in

trinsic instabilities in dense active suspensions—can alter the system’s phase even at fixed activity levels, effectively shifting the critical activity threshold for structural transitions.

Generalized Hydrodynamic model: We consider a coarse-grained hydrodynamic model to describe the collective dynamics of a two-dimensional dense bacterial suspension [8]:

$$\frac{\partial \mathbf{u}}{\partial t} + \lambda_0 \mathbf{u} \cdot \nabla \mathbf{u} = -\nabla p - (\alpha + \beta |u|^2) \mathbf{u} + \Gamma_0 \nabla^2 \mathbf{u} - \Gamma_2 \nabla^4 \mathbf{u} \quad (1)$$

$$\nabla \cdot \mathbf{u} = 0$$

where $\mathbf{u}(\mathbf{x}, t)$ is the coarse-grained velocity field. The divergence-free condition enforces the incompressibility of \mathbf{u} . $p(\mathbf{x}, t)$ is the pressure field. The coefficient λ_0 encodes the effects of different swimmer types: $\lambda_0 > 1$ corresponds to pusher-type swimmers, while $\lambda_0 < 1$ corresponds to puller-type swimmers. The Toner-Tu coefficients (α, β) describe the polar ordering in self-propelled particle systems [3]: for values of $\alpha < 0 (> 0)$ the term αu injects (dissipates) energy and $\beta > 0$ dissipates energy while ensuring numerical stability. Together, they define a characteristic velocity scale, $v = \sqrt{-\alpha/\beta}$, for polar-ordered motion. The (Γ_0, Γ_2) term has the structure of the Swift-Hohenberg equation [31]. With $\Gamma_0 < 0$ and $\Gamma_2 > 0$, this term inherently drives the system towards a linear instability at length scales, $\Lambda = 2\pi \sqrt{\frac{2\Gamma_2}{\Gamma_0}}$. It is the interplay between these terms that leads to chaotic, self-sustaining, turbulent-like flow patterns.

Simulation details: To numerically solve Eqs. (1), we employed a de-aliased pseudo-spectral algorithm with periodic boundary conditions in space. We perform two-dimensional simulations in a square domain of size 160×160 and grid resolution 4096×4096 , ensuring sufficient resolution for capturing fine-scale features. Time integration was performed using the second-order integrating factor method (IFRK2) with a time step of $\Delta t = 2 \times 10^{-4}$. The simulations were initialized with random initial conditions and in all simulation cases, we set the parameters fixed unless otherwise stated, $\lambda_0 = 3.5$, $\beta = 0.5$, $\Gamma_2 = 9 \times 10^{-4}$, $\Gamma_0 = 4.5 \times 10^{-2}$. These values are chosen based on previous studies that align with experimentally accessible regimes [20]. For more details, see section S1. To investigate the role of activity, we systematically vary the parameter α between -9 to -1.

Spatial distribution of vortex centers: We show in Fig. 1 (a) and (b) the plots of vorticity field $\omega(\mathbf{x}, t) = \nabla \times \mathbf{u}(\mathbf{x}, t)$ for different values of the activity parameter α . The field ω undergoes a structural transformation as α decreases, with large-scale spatial inhomogeneities becoming more prominent at lower α or, equivalently, higher activity. These inhomogeneities are apparent from the long-range correlations in the vorticity field as seen in Figs. 1(b) and 1(d). In active matter systems, such large-scale spatial inhomogeneities are indicative of giant number fluctuations where the standard deviation (Δn) of the number of active particles (n) grows anomalously large and scales as $\Delta n \sim n^\delta$, with the exponent δ reaching values as high as 1 in two dimensions [32–34]. In the asymptotic limit of n , $\delta = 0.5$ for systems in equilibrium and away from continuous phase transitions. In analogy, in active turbulence, we find giant number fluctuations of the vortex centers. To quantify the fluctuations in the number of vortices, we

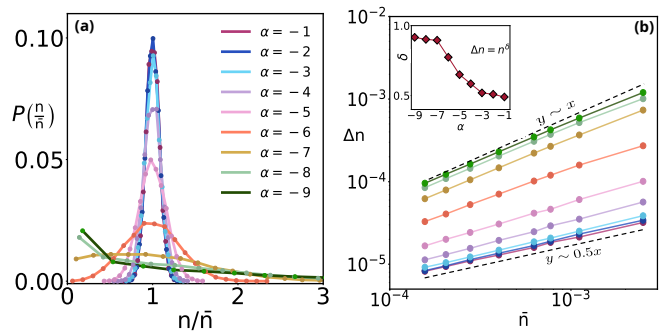


FIG. 2: (a) Probability distribution functions (PDF) of the normalized vortex count (n/\bar{n}) in subdomains of fixed linear size ℓ for different activity values. As $|\alpha|$ increases the distributions broaden and their maxima shift from $n/\bar{n} \simeq 1$ toward lower values, indicating that typical subdomains contain fewer vortex centers, while strong fluctuations become more likely. (b) Standard deviation Δn of the number of vortex centers within subregions is plotted against the corresponding mean \bar{n} as the subregion size ℓ increases. The scaling behavior $\Delta n \sim \bar{n}^\delta$ reveals the presence of giant number fluctuations for $\alpha < \alpha_c$. Inset: the scaling exponent δ is plotted as a function of the activity parameter α , showing that fluctuations become increasingly pronounced (larger δ) with higher activity.

compute the average number of vortices \bar{n} and the corresponding variance, Δn within a subregion of size ℓ^2 . In Fig. 2(a), we plot the probability distribution (PDF) of n around its mean for different α , in a given subregion. We note that for decreasing α , the $P(n)$ broadens, indicating stronger fluctuations in the number of vortex centers. In Fig. 2(b) we plot Δn versus \bar{n} for different activities and find that $\Delta n \sim \bar{n}^\delta$, with $\delta \simeq 0.5$ for $\alpha \geq -5$ and $\delta > 0.5$ for $\alpha < -5$. The values of δ approach 1 for very large $|\alpha|$, see inset of Fig. 2(b). Notably, the transition of δ at a critical value of the activity parameter, $\alpha_c = -5$, matches with the previously identified critical activity by the group of Ray [19, 26] through the onset of universality in energy spectra, increased intermittency, and other hallmarks of turbulent transitions. Note that with increasing activity, although the vorticity at individual vortex centers increases, the total number of such centers decreases S2(b).

The methodology for identifying vortex centers is provided in section S2. While the fluctuations in number reflect statistical deviations, a more structural perspective on the spatial inhomogeneity of vortex centers is offered by Voronoi tessellation. The results of this analysis are consistent with the emergence of giant number fluctuations at high activity levels (see section S3).

Emergence of local ordering : This statistical signature of inhomogeneity naturally raises the question: what changes in the underlying flow field are responsible for this transition? To address this, we closely examine the structure of the vorticity and velocity fields. For $\alpha < \alpha_c$, there are a few large vortical regions of the size $\sim 25\Lambda$ characterized by low or nearly vanishing vorticity (see Fig. 1(d)) interspersed with vortical regions of the size $\mathcal{O}(\Lambda)$. In Fig 3(b), we plot the velocity streamlines corresponding to these large vortical regions of vanishing vorticity and note that they are highly aligned,

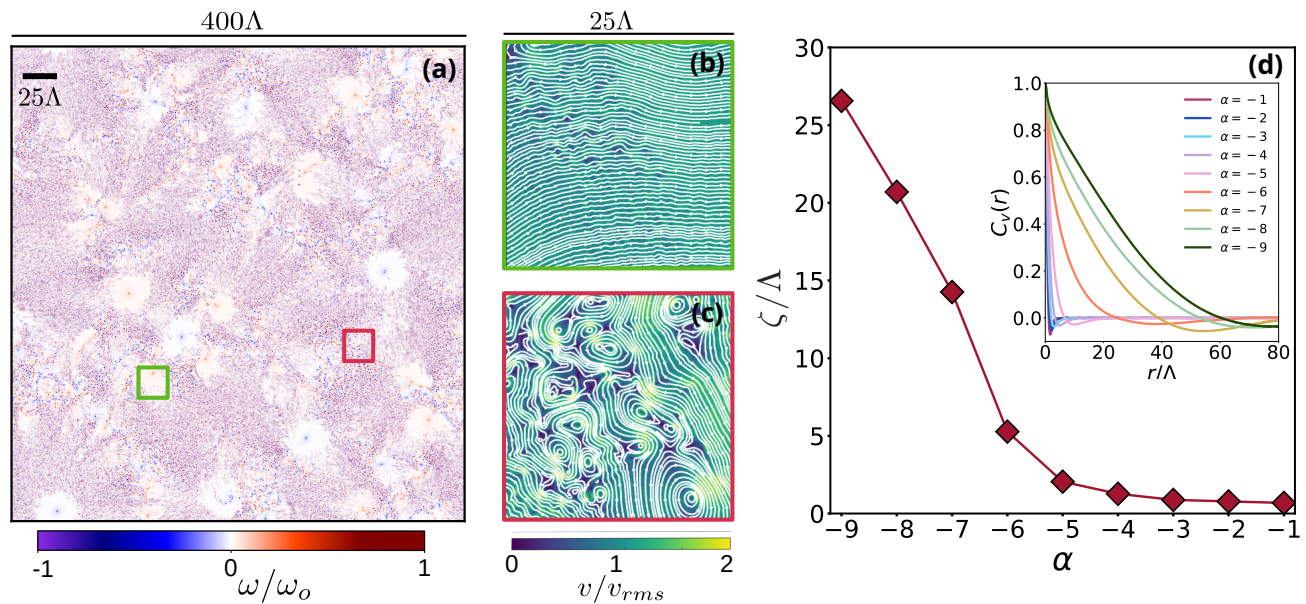


FIG. 3: (a) Vorticity field for the entire domain for $\alpha = -9$, with the scale bar indicating a length scale of 25Λ . (b) and (c) show the velocity streamlines overlaid on the velocity magnitude for a domain of size 25Λ . (d) The normalized velocity correlation length ζ versus α . *Inset*: The spatial velocity correlation function, defined as $C_v(r) = \langle \mathbf{u}(\mathbf{r}_0) \cdot \mathbf{u}(\mathbf{r}_0 + \mathbf{r}) \rangle$ is shown as a function of distance r for increasing values of $|\alpha|$. The velocity correlation length ζ is extracted by fitting the decay of $C_v(r)$ to an exponential form $C_v(r) \sim e^{-r/\zeta}$. For $\alpha > \alpha_c$, the normalized correlation length ξ/Λ remains close to one, whereas it increases significantly for $\alpha < \alpha_c$, indicating the emergence of long-range velocity correlations in the high-activity regime.

indicating local ordering. This contrasts sharply with other regions of the same field Fig 3(c), where the flow remains disordered and lacks directional alignment. Furthermore, in Fig 3(d) we plot velocity correlation $C_v(r) = \langle \mathbf{u}(\mathbf{r}_0) \cdot \mathbf{u}(\mathbf{r}_0 + \mathbf{r}) \rangle$ versus r and see that there is a sharp transition followed by a monotonic increase in correlation length, ζ , for $\alpha < \alpha_c$. For sufficiently negative α (e.g., $\alpha \lesssim -6$), the spatial velocity correlation length reaches up to $\mathcal{O}(10\Lambda)$ and for $\alpha = -9$ we find $\zeta \simeq 25\Lambda$, consistent with the lengths of the large vortical regions seen in Fig. 1 (b). For $\alpha > \alpha_c$, we note from Fig. 1 (a) and (c), the largest vortical structures are $\sim \mathcal{O}(\Lambda)$ and velocity streamlines are chaotic throughout domain, see Fig. S2(a). Signatures of local ordering can also be seen in the PDF of the velocity field: we plot in Fig. 4(a) the PDF of a component of the velocity field for different activities and observe that the PDF transitions from a unimodal distribution centered at $\langle u \rangle = 0$ for $\alpha > \alpha_c$ to a bimodal for $\alpha < \alpha_c$. The two peaks in the bimodal state progressively approach $\pm \sqrt{\frac{\alpha}{\beta}}$, consistent with the predictions of the Toner-Tu model for self-propelled active systems. This highlights competition between active alignment-induced ordering Toner-Tu terms and spatial modulation introduced by higher-order gradient terms.

The global phase behavior is not dictated by a single control parameter but instead emerges from a balance between multiple energetically distinct contributions. The first is the energy associated with activity-driven motion, quantified as $E_{\text{active}} = \frac{v^2}{2}$. The second arises from the destabilizing active stresses introduced by the generalized Swift–Hohenberg-like term, which generates intrinsic instabilities and injects energy

into the system at intermediate length scales. The energy associated with this contribution is given by $E_\Lambda = \frac{|\Gamma_0^3|}{\Gamma_2}$. The third component is the kinetic energy of the flow, $E_{\text{kin}} (\equiv \int_{\mathbf{x} \in L^2} \frac{1}{2} \mathbf{u} \cdot \mathbf{u} d\mathbf{x})$. This energetic framework allows us to define an effective order parameter, ϕ , that captures the interplay between these different forms of energy input and transfer.

$$\phi = E_{\text{active}} - E_\Lambda - E_{\text{kin}},$$

We hypothesize that the relative magnitudes of E_{active} , E_Λ , and E_{kin} determine the qualitative state of the system — whether it exhibits local ordering identified by long correlation lengths or remains in a disordered phase. For $\alpha < \alpha_c$, the order parameter ϕ becomes positive, indicating that the active energy E_{active} dominates over other contributions. This leads to a breakdown of homogeneity and the emergence of local ordering. In contrast, $\phi < 0$ corresponds to a homogeneous, disordered state where active energy is insufficient to induce such organization, Fig. 4(b).

Instability Growth Timescale as an Alternative Control Parameter: Having explored the role of the activity parameter α , which sets a characteristic timescale $\tau_\alpha = 1/|\alpha|$ for the growth of polar order, we now turn to a complementary perspective: fixing α and varying the timescale associated with the growth of instabilities, defined as $\tau_\Gamma = \Gamma_2/|\Gamma_0|^2$. In previous sections, τ_Γ was kept fixed while α was varied to investigate its impact on the emergence of large-scale structures. However, since both parameters control the growth rate of perturbations [8], we now ask whether varying τ_Γ at fixed α can produce effects analogous to varying α at fixed τ_Γ .

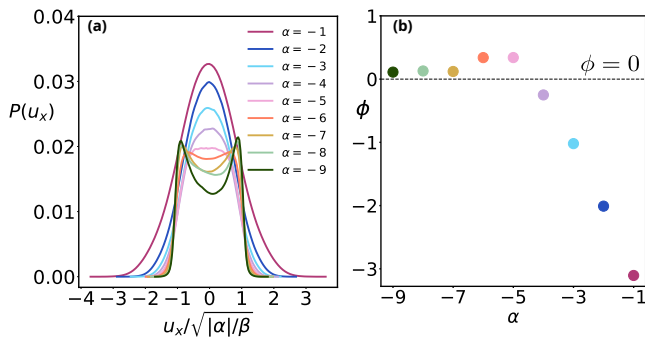


FIG. 4: (a) Probability distribution function of the a velocity component u_x for different values activity α . A transition from a unimodal to a bimodal distribution is observed as α decreases beyond the critical point α_c . (b) The order parameter $\phi = E_{\text{active}} - E_{\Lambda} - E_{\text{kin}}$, is plotted as a function of α . ϕ is positive below α_c and becomes negative above it, reflecting the onset of the transition.

We fix $\alpha = -4$, below the critical threshold α_c , and varied the instability growth timescale $\tau_{\Gamma} = \Gamma_2/|\Gamma_0|^2$ by adjusting $|\Gamma_0|$. For increased τ_{Γ} (i.e., smaller $|\Gamma_0|$), the energy spectra shown in Fig. 5 exhibit a power-law scaling of the form $E(k) \sim k^{-3/2}$, qualitatively similar to that observed for large $|\alpha|$ ($\alpha < \alpha_c$). Conversely, reducing τ_{Γ} by increasing $|\Gamma_0|$ produces spectra resembling those at smaller $|\alpha|$, (increased τ_{α}). Notably, the order parameter ϕ sharply captures this transition, changing sign in correspondence with the shift in flow structure (Fig. 5, inset).

Furthermore, to validate the generality of the order parameter, we perform two complementary simulations. First, we take the locally ordered state $\alpha = -8$ and decrease Γ_2 to 3.6×10^{-5} , hence decreasing τ_{Γ} and the system goes into a disordered state with $\phi < 0$. In the second simulation, we choose a disordered state $\alpha = -3$ and increased τ_{Γ} by increasing Γ_2 to 1.8×10^{-4} and the system goes into a locally ordered state with $\phi > 0$ (Fig. S5). These results suggest that α and τ_{Γ} both influence the system's instability dynamics and spectral properties, though the precise relationship between them remains to be clarified.

Discussion: Our study uncovers a rich interplay between microscopic activity and emergent large-scale structures in the system's flow dynamics. The results from our various analyses collectively point to a transition from disorder to a locally ordered state, as the magnitude of activity increases, through competing physical processes. Crucially, this structural transition is accompanied by the emergence of giant number fluctuations in the distribution of vortex centers, pointing towards the inhomogeneous distribution of these vortex centers in space. This structural inhomogeneity emerges from the interplay between the ordering dynamics and the inherent tendency for pattern formation. The Toner-Tu terms promote local ordering due to long-range polar alignment [3]. In contrast, the Swift-Hohenberg term introduces a counteracting influence, driving the system toward spatially chaotic structures [31]. With the increase in activity, the local polar ordering emerges and strengthens, manifesting as a marked increase in velocity correlation length. A key signature of this transition is the

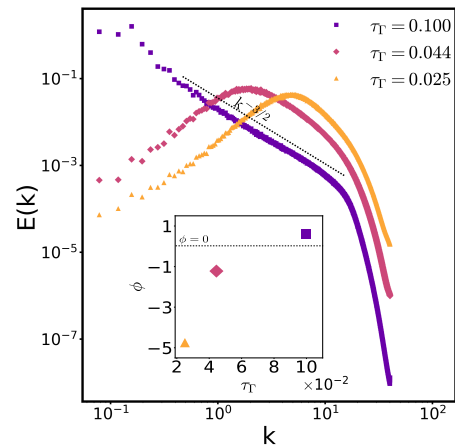


FIG. 5: The energy spectra by varying the instability growth timescale ($\tau_{\Gamma} = \frac{\Gamma_2}{\Gamma_0^2}$) by varying Γ_0 for fixed $\alpha = -4$, $\Gamma_2 = 9 \times 10^{-5}$, $\beta = 0.5$ and $\lambda_0 = 3.5$. Inset: The corresponding energy-based order parameter ϕ is plotted as a function of τ_{Γ} , showing a sign reversal that is consistent with a transition.

evolution of the velocity distribution: from unimodal Gaussian at low activity to bimodal at higher activity. Interestingly, the onset of bimodality in the velocity distribution coincides with the emergence of anomalous diffusion, as observed experimentally in bacterial turbulence by [35, 36] and reported in simulations by [26], suggesting a potential connection between transport behavior and changes in velocity statistics.

Notably, we find that this transition is sensitive to the strength of the higher-order derivative terms Γ_0 and Γ_2 , hence E_{Λ} . This transition is robustly captured by the order parameter ϕ , which switches sign in accordance with the onset of structural inhomogeneity. Together, these findings establish a physically grounded picture of how active stresses, alignment dynamics, and higher-order instabilities conspire to shape the multiscale organization of flows in dry active systems. The system's transition from disorder to local order is not governed by a single control parameter but rather emerges from the nonlinear coupling of energetically distinct processes and their sensitivity to model parameters. Future investigations could extend this framework to three-dimensional active flows, where the interplay between alignment and higher-order instabilities may lead to qualitatively new regimes of spatiotemporal organization. Incorporating density fluctuations and nematic order could further elucidate the coupling between flow structure and internal degrees of freedom [37, 38]. On the experimental side, dense suspensions of fast-swimming bacteria or active colloids with tunable alignment and instability parameters offer promising platforms to probe the predicted transition.

ACKNOWLEDGMENTS

We thank S. Mukherjee, S. Ray, and P. Perlekar for helpful discussions. These simulations were performed on the

IITH NVIDIA V100 GPU cluster, Param Seva supercomputers through the National Supercomputing Mission, and the IITH Kanad clusters. KK acknowledges the TCS Foundation for financial support through the Research fellowship program (TCS/17/23-24/P49) KVK is grateful for funding from

the Simons' Collaboration on Wave Turbulence (award No. 651459). A. G. acknowledges SERB-DST (India) Projects MTR/2022/000232, CRG/2023/007056-G, DST (India) grant no. DST/NSM/R&D_HPC.Applications/2021/05 and grant no. SR/FST/PSI-215/2016, and IITH for Seed Grant No. IITH/2020/09 for financial support.

-
- [1] Ricard Alert, Jaume Casademunt, and Jean-François Joanny. Active turbulence. *Annual Review of Condensed Matter Physics*, 13(1):143–170, 2022.
- [2] M Cristina Marchetti, Jean-François Joanny, Sriram Ramaswamy, Tanniemola B Liverpool, Jacques Prost, Madan Rao, and R Aditi Simha. Hydrodynamics of soft active matter. *Reviews of modern physics*, 85(3):1143–1189, 2013.
- [3] John Toner, Yuhai Tu, and Sriram Ramaswamy. Hydrodynamics and phases of flocks. *Annals of Physics*, 318(1):170–244, 2005.
- [4] Luca Giomi, Mark J Bowick, Xu Ma, and M Cristina Marchetti. Defect annihilation and proliferation in active nematics. *Physical review letters*, 110(22):228101, 2013.
- [5] Martin James, Dominik Anton Suchla, Jörn Dunkel, and Michael Wilczek. Emergence and melting of active vortex crystals. *Nature communications*, 12(1):5630, 2021.
- [6] Sandrine Ngo, Anton Peshkov, Igor S Aranson, Eric Bertin, Francesco Ginelli, and Hugues Chaté. Large-scale chaos and fluctuations in active nematics. *Physical review letters*, 113(3):038302, 2014.
- [7] Pau Guillamat, Jordi Ignés-Mullol, and Francesc Sagués. Control of active liquid crystals with a magnetic field. *Proceedings of the National Academy of Sciences*, 113(20):5498–5502, 2016.
- [8] Henricus H Wensink, Jörn Dunkel, Sebastian Heidenreich, Knut Drescher, Raymond E Goldstein, Hartmut Löwen, and Julia M Yeomans. Meso-scale turbulence in living fluids. *Proceedings of the national academy of sciences*, 109(36):14308–14313, 2012.
- [9] Andrey Sokolov, Igor S Aranson, John O Kessler, and Raymond E Goldstein. Concentration dependence of the collective dynamics of swimming bacteria. *Physical review letters*, 98(15):158102, 2007.
- [10] Vincent A Martinez, Eric Clément, Jochen Arlt, Carine Douarche, Angela Dawson, Jana Schwarz-Linek, Adama K Creppy, Viktor Škultéty, Alexander N Morozov, Harold Auradou, et al. A combined rheometry and imaging study of viscosity reduction in bacterial suspensions. *Proceedings of the National Academy of Sciences*, 117(5):2326–2331, 2020.
- [11] Pau Guillamat, Jordi Ignés-Mullol, and Francesc Sagués. Taming active turbulence with patterned soft interfaces. *Nature communications*, 8(1):564, 2017.
- [12] Da Wei, Yaochen Yang, Xuefeng Wei, Ramin Golestanian, Ming Li, Fanlong Meng, and Yi Peng. Scaling transition of active turbulence from two to three dimensions. *Advanced Science*, 11(38):2402643, 2024.
- [13] Cecilia Rorai, Federico Toschi, and Ignacio Pagonabarraga. Coexistence of active and hydrodynamic turbulence in two-dimensional active nematics. *Physical Review Letters*, 129(21):218001, 2022.
- [14] Charles W Wolgemuth. Collective swimming and the dynamics of bacterial turbulence. *Biophysical journal*, 95(4):1564–1574, 2008.
- [15] Christopher Dombrowski, Luis Cisneros, Sunita Chatkaew, Raymond E Goldstein, and John O Kessler. Self-concentration and large-scale coherence in bacterial dynamics. *Physical review letters*, 93(9):098103, 2004.
- [16] Amin Doostmohammadi and Julia M Yeomans. Coherent motion of dense active matter. *The European Physical Journal Special Topics*, 227:2401–2411, 2019.
- [17] Sanjay CP and Ashwin Joy. Friction scaling laws for transport in active turbulence. *Physical Review Fluids*, 5(2):024302, 2020.
- [18] Berta Martínez-Prat, Ricard Alert, Fanlong Meng, Jordi Ignés-Mullol, Jean-François Joanny, Jaume Casademunt, Ramin Golestanian, and Francesc Sagués. Scaling regimes of active turbulence with external dissipation. *Physical Review X*, 11(3):031065, 2021.
- [19] Siddhartha Mukherjee, Rahul K Singh, Martin James, and Samriddhi Sankar Ray. Intermittency, fluctuations and maximal chaos in an emergent universal state of active turbulence. *Nature Physics*, 19(6):891–897, 2023.
- [20] Kolluru Venkata Kiran, Anupam Gupta, Akhilesh Kumar Verma, and Rahul Pandit. Irreversibility in bacterial turbulence: Insights from the mean-bacterial-velocity model. *Physical Review Fluids*, 8(2):023102, 2023.
- [21] Rahul Pandit and Kolluru Venkata Kiran. Particles and fields in minimal hydrodynamic models for active turbulence. *Europhysics Letters*, 150(1):13001, apr 2025.
- [22] Kolluru Venkata Kiran, Kunal Kumar, Anupam Gupta, Rahul Pandit, and Samriddhi Sankar Ray. Onset of intermittency and multiscaling in active turbulence. *Physical Review Letters*, 134(8):088302, 2025.
- [23] Rajesh Ramaswamy and Frank Jülicher. Activity induces traveling waves, vortices and spatiotemporal chaos in a model actomyosin layer. *Scientific reports*, 6(1):20838, 2016.
- [24] Moritz Linkmann, Guido Boffetta, M Cristina Marchetti, and Bruno Eckhardt. Phase transition to large scale coherent structures in two-dimensional active matter turbulence. *Phys. Rev. Lett*, 122(21):214503, 2019.
- [25] Moritz Linkmann, M Cristina Marchetti, Guido Boffetta, and Bruno Eckhardt. Condensate formation and multiscale dynamics in two-dimensional active suspensions. *Phys. Rev. E*, 101(2):022609, 2020.
- [26] Siddhartha Mukherjee, Rahul K Singh, Martin James, and Samriddhi Sankar Ray. Anomalous diffusion and lévy walks distinguish active from inertial turbulence. *Physical Review Letters*, 127(11):118001, 2021.
- [27] L Puggioni, G Boffetta, and S Musacchio. Giant vortex dynamics in confined bacterial turbulence. *Physical Review E*, 106(5):055103, 2022.
- [28] Andrey Sokolov and Igor S Aranson. Reduction of viscosity in suspension of swimming bacteria. *Physical review letters*, 103(14):148101, 2009.
- [29] Hüseyin Kurtuldu, Jeffrey S Guasto, Karl A Johnson, and Jerry P Gollub. Enhancement of biomixing by swimming al-

- gal cells in two-dimensional films. *Proceedings of the National Academy of Sciences*, 108(26):10391–10395, 2011.
- [30] Juan P Hernandez-Ortiz, Christopher G Stoltz, and Michael D Graham. Transport and collective dynamics in suspensions of confined swimming particles. *Physical review letters*, 95(20):204501, 2005.
- [31] Jack Swift and Pierre C Hohenberg. Hydrodynamic fluctuations at the convective instability. *Physical Review A*, 15(1):319, 1977.
- [32] Hugues Chat e. Dry aligning dilute active matter. *Annual Review of Condensed Matter Physics*, 11(1):189–212, 2020.
- [33] Vijay Narayan, Sriram Ramaswamy, and Narayanan Menon. Long-lived giant number fluctuations in a swarming granular nematic. *Science*, 317(5834):105–108, 2007.
- [34] Yaouen Fily and M Cristina Marchetti. Athermal phase separation of self-propelled particles with no alignment. *Physical review letters*, 108(23):235702, 2012.
- [35] Dhananjay Gautam, Hemlata Meena, Saravanan Matheshwaran, and Sivasurender Chandran. Harnessing density to control the duration of intermittent l evy walks in bacterial turbulence. *Physical Review E*, 110(1):L012601, 2024.
- [36] Gil Ariel, Amit Rabani, Sivan Benisty, Jonathan D Partridge, Rasika M Harshey, and Avraham Be’Er. Swarming bacteria migrate by l evy walk. *Nature communications*, 6(1):8396, 2015.
- [37] SumeshP Thampi and JuliaM Yeomans. Active turbulence in active nematics. *The European Physical Journal Special Topics*, 225:651–662, 2016.
- [38] Sumesh P Thampi, Ramin Golestanian, and Julia M Yeomans. Velocity correlations in an active nematic. *Physical review letters*, 111(11):118101, 2013.
- [39] Pope Sb. Turbulent flows. *Cambridge University Pres*, 2000.
- [40] John Weiss. The dynamics of enstrophy transfer in two-dimensional hydrodynamics. *Physica D: Nonlinear Phenomena*, 48(2-3):273–294, 1991.
- [41] Dalila Elhma idi, Antonello Provenzale, and Armando Babiano. Elementary topology of two-dimensional turbulence from a lagrangian viewpoint and single-particle dispersion. *Journal of Fluid Mechanics*, 257:533–558, 1993.
- [42] K Osawa, Y Minamoto, M Shimura, and M Tanahashi. Voronoi analysis of vortex clustering in homogeneous isotropic turbulence. *Physics of Fluids*, 33(3), 2021.

SUPPLEMENTARY MATERIAL

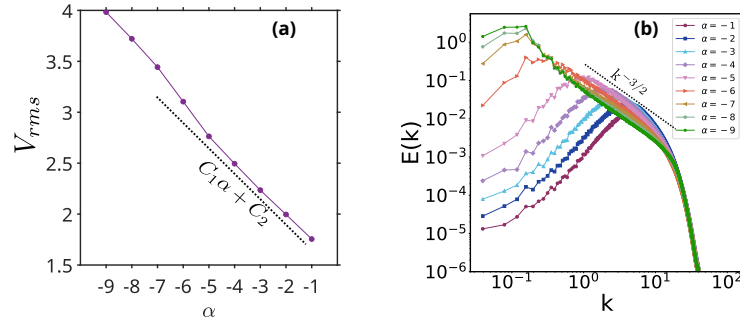
S1. NUMERICAL METHODS

To numerically solve Eq: 1 in main text, we have used vorticity-stream function formalism [39]. Taking curl of Eq: 1 and using from incompressibility condition in 2d we get,

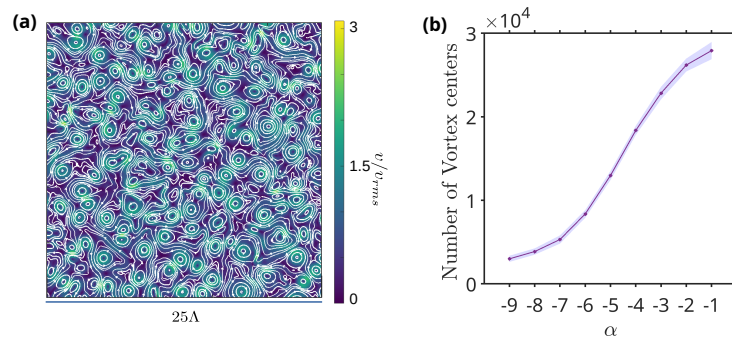
$$\frac{\partial \omega}{\partial t} + \lambda_0 \mathbf{u} \cdot \nabla \omega = -\alpha \omega - \beta \nabla \times (|\mathbf{u}|^2 \mathbf{u}) + \Gamma_0 \nabla^2 \omega - \Gamma_2 \nabla^4 \omega; \quad (\text{S2})$$

where ω is $\nabla \times \mathbf{u}$.

The simulations were performed on a square domain of size 160×160 with a uniform grid resolution of 4096×4096 . This corresponds to a grid spacing of $dx = 0.04$, which sets the smallest resolvable length scale in the simulation. This grid spacing is significantly smaller than the characteristic length scale, $\Lambda = 2\pi \sqrt{\frac{2\Gamma_2}{\Gamma_0}} = 0.4$. It is also smaller than the typical dissipation length scale, ensuring that small-scale structures and the fine details of the flow are well captured. The choice of domain size was made to be much larger than the maximum velocity correlation length scale for the highest activity parameter ($\alpha = -9$) used in our simulations. This ensures that the system can develop a broad range of scales without being artificially constrained by the domain boundaries and forming condensates. This setup allows the dynamics to evolve naturally, capturing both the large-scale collective motion and the finer-scale turbulent structures present in active systems. We have used the FFTW module for Fourier transforms for the pseudo-spectral method. The time marching is done using the second-order integrating factor method, where the stiff linear part is handled exactly through the integrating factor, improving stability. In the time step, $dt = 2 \times 10^{-4}$ for up to 2×10^5 iterations, all the statistical averages are taken over 50 snapshots after the system reaches a steady state.



Supplementary Figure S1: (a) V_{rms} increases with activity, (increasing $-\alpha$). (b) Energy spectra for different α , showing power scaling for $\alpha < -\alpha_c$.



Supplementary Figure S2: (a) Velocity streamlines overlaid on the velocity magnitude are shown for $\alpha = -1$ in a $25\Lambda \times 25\Lambda$ domain, highlighting flow structures predominantly governed by the length scale $\mathcal{O}(\Lambda)$. The color bar is normalized by u_{rms} .

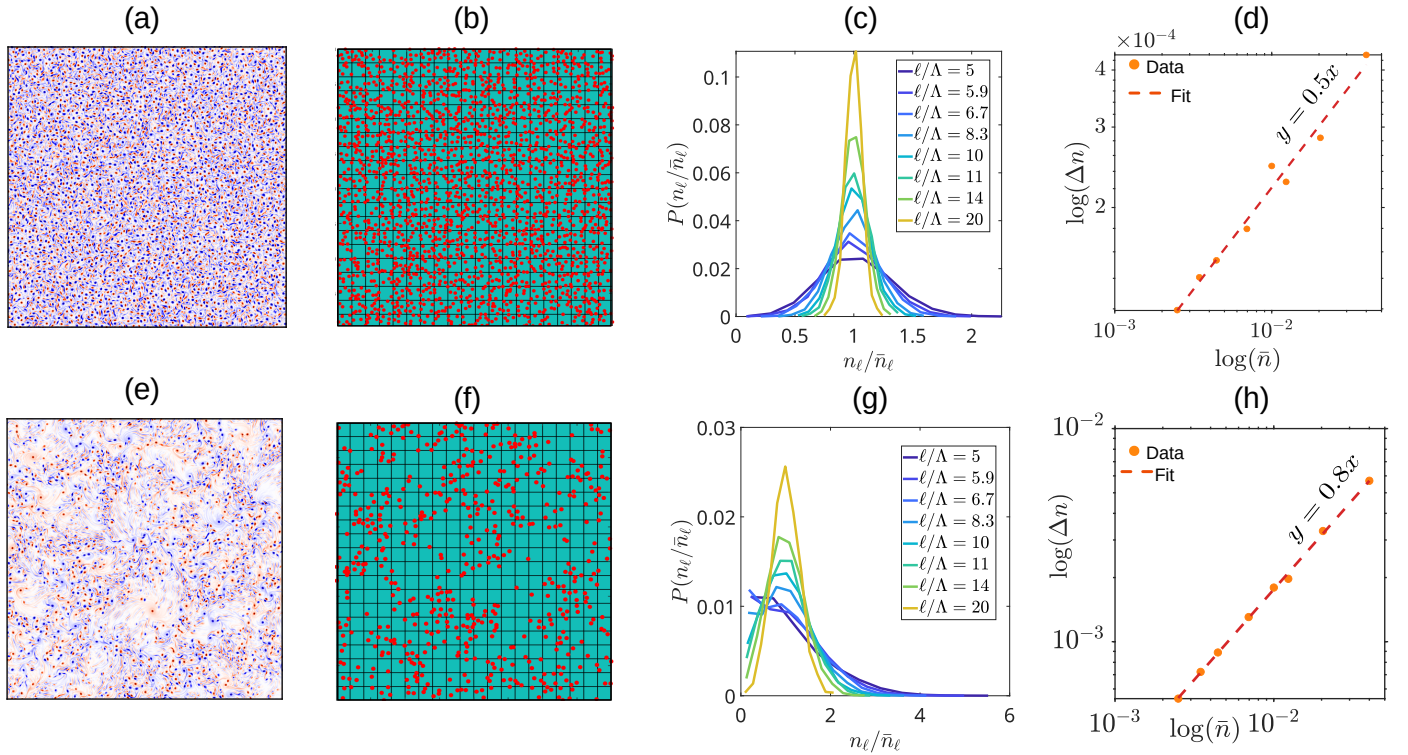
(b) The time-averaged number of identified vortex centers as a function of α , showing a decrease in the number of distinct vorticity centers with increasing activity. The shaded region represents the fluctuations (standard deviation) over time.

S2. DETAILS OF EXTRACTION OF VORTEX CENTERS

For the number fluctuation analysis, from each snapshot, we extracted the intense vorticity regions by applying a threshold on the Okubo-Weiss parameter. The Okubo-Weiss parameter, defined as $Q = \frac{\omega^2 - \sigma^2}{4}$, where $\sigma^2 = \frac{1}{2} \sum_{ij} (\partial_i u_j + \partial_j u_i)^2$ with $i, j = 1, 2$ can be used to determine the vorticity-dominated and strain dominated regions [40, 41]. We extracted the regions with $Q < Q_t$. Within each of these regions that are connected vorticity-dominated patches, we estimated the vortex center using an intensity-weighted centroid, where the vorticity field serves as the weighting function. If $((x_i, y_i))$ denote the coordinates of the (i^{th}) grid in a region, and (w_i) is the corresponding vorticity magnitude at that location, then the centroid $((x_c, y_c))$ is computed as:

$$x_c = \frac{\sum_i x_i \cdot w_i}{\sum_i w_i}, \quad y_c = \frac{\sum_i y_i \cdot w_i}{\sum_i w_i}. \quad (\text{S3})$$

The identified centroids are then used in further statistical analyses, such as computing number fluctuations across subdomains of varying size (discussed in the main text, see Fig.S3), Voronoi analysis (discussed in the next section). To analyze the distribution of intense vortices for each time step, the system is divided into subregions of area ℓ^2 , and estimate the number of vortex centers n in each subregion, the average number of vortex centers \bar{n} and the standard deviation Δn , all normalized by the total number of vortex centers. The subregion size is varied over a range with $\ell \in [5\Lambda, 20\Lambda]$.



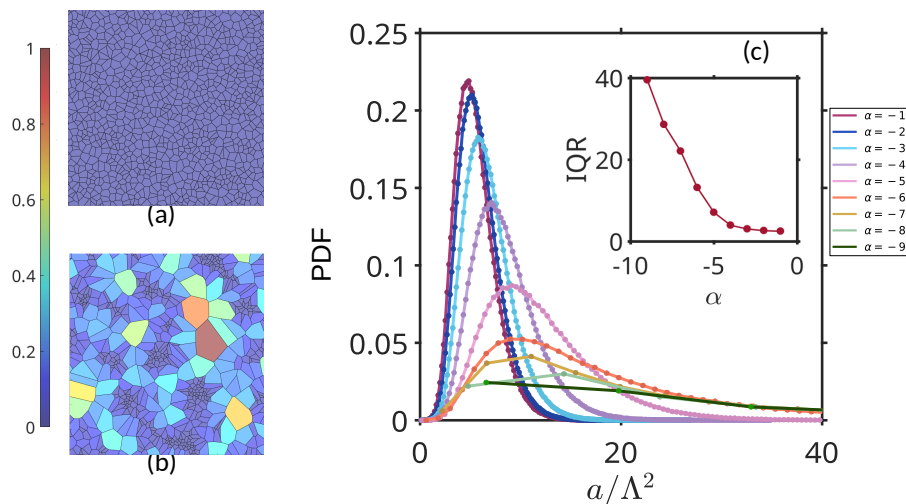
Supplementary Figure S3: (a) and (d) show the vorticity field for weak ($\alpha = -1$) and strong ($\alpha = -6$) activity, respectively, revealing a transition from spatially disordered vortex structures to highly structured patterns with dense vortical regions and zero or less vorticity regions. (b) and (e) display the corresponding extracted vortex centers at a single time step, obtained by identifying regions below a threshold in the Okubo–Weiss parameter and computing their intensity-weighted centroids. (c) and (f) show the probability distribution functions of the number of vortex centers n_ℓ within subdomains of varying size ℓ , with $\ell \in [5\Lambda, 20\Lambda]$, highlighting the change in spatial homogeneity. (g) and (h) present the number fluctuations Δn as a function of the average \bar{n}_ℓ , respectively, for the two activity levels. For low activity ($\alpha = -1$), $\Delta n \sim \bar{n}_\ell^{0.5}$, indicating homogeneous distribution, while for high activity ($\alpha = -6$), the scaling approaches $\Delta n \sim \bar{n}_\ell^{0.8}$, consistent with inhomogeneity in vortex centers distribution.

S3. VORONOI ANALYSIS OF VORTEX CENTER DISTRIBUTION

To further quantify the spatial inhomogeneity in the distribution of vortex centers, we performed a Voronoi tessellation analysis. A Voronoi tessellation divides the domain into polygonal cells such that each cell contains exactly one vortex center, and every point in a given cell is closer to its associated center than to any other. This method provides a geometric way to measure the local spacing between vortex centers and is widely used to detect clustering or depletion in point patterns[42]. By calculating the area of each Voronoi cell, we obtained a distribution of cell areas that serves as a proxy for the local density of vortex centers. In a spatially homogeneous system, Fig.S4(a), the distribution of Voronoi cell areas is expected to be narrow and peaked. However, for increasing activity, we observed a broadening of this distribution, S4(b), indicating the emergence of clustering and void-like regions, Fig.S4(c). In particular, our results show that for activity levels beyond ($\alpha_c = -5$), the Voronoi area distribution departs significantly from that Gaussian distribution. This transition reflects the development of spatial inhomogeneity in the vortex center positions, consistent with our findings from the number fluctuation analysis. The inset displays the interquartile range (IQR), which serves as a measure of the spread in the area distribution. The IQR is defined as the difference between the 75th percentile (Q_3) and the 25th percentile (Q_1) of the distribution:

$$IQR = Q_3 - Q_1$$

The IQR effectively captures the range within which the central 50% of the data fall. The IQR of area distribution increases with activity, indicating that the distribution of Voronoi areas becomes more spread out at higher activity levels.



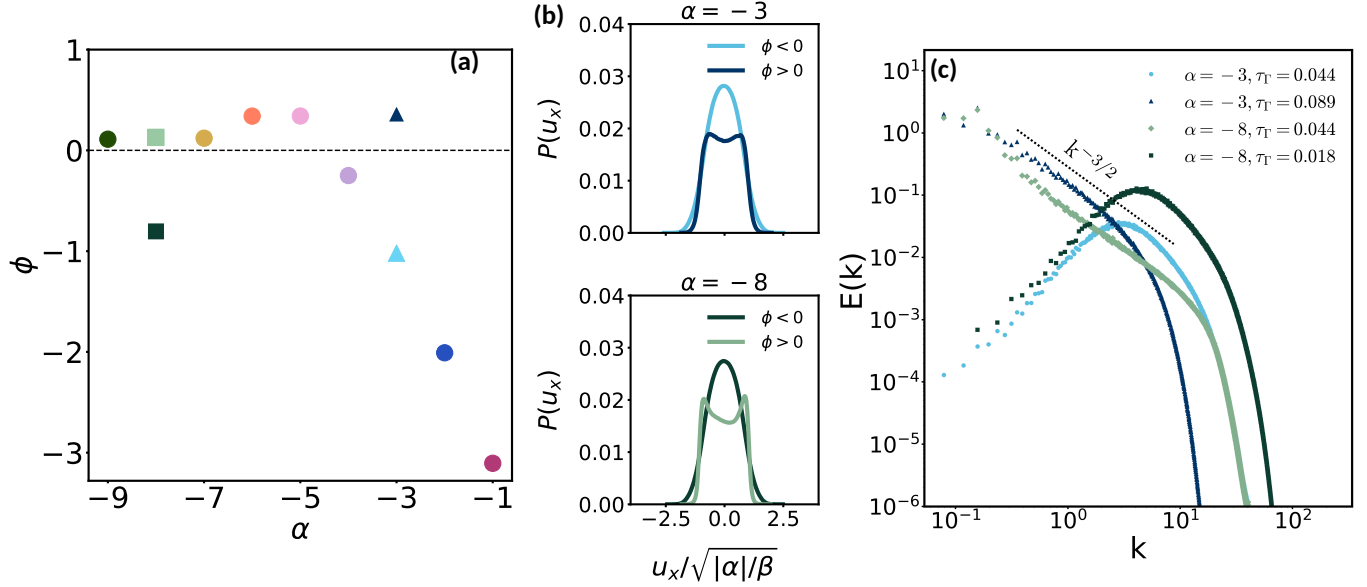
Supplementary Figure S4: (a) and (b) represent the area constructed by Voronoi tessellation based on the filtered vortex index for $\alpha = -1$ and $\alpha = -8$, respectively. (c) The probability distribution of the areas of these Voronoi polygons. The inset shows the interquartile range (IQR) of the distribution

S4. ORDER PARAMETER

We explored additional parameter regimes by varying the strength of the higher-order term Γ_2 , which modulates the influence of the Swift-Hohenberg instability. Our results underscore the critical role of the interplay between two competing physical mechanisms: the Toner-Tu term, which promotes local alignment and polar order, and the Swift-Hohenberg term, which favors spatial modulation and destabilizes uniform configurations.

This competition governs the emergence and breakdown of mesoscale structures. For instance, at a fixed activity level $\alpha = -3$, increasing Γ_2 leads to a transition from a disordered to an ordered state, as reflected by a change in the sign of the order parameter ϕ and a corresponding shift in the velocity distribution from unimodal to bimodal, Fig.S5(b). Similarly, at $\alpha = -8$, decreasing Γ_2 results in a breakdown of local order, with ϕ switching from positive to negative and the velocity statistics reverting to a unimodal form, Fig.S5(c).

These findings demonstrate that the onset of local ordering is not governed solely by activity strength, but emerges from a balance between active alignment and the intrinsic instability of the system. The velocity distribution and order parameter ϕ serve as sensitive diagnostics of this balance, capturing the transition in the system's collective dynamics.



Supplementary Figure S5: (a) Order parameter ϕ as a function of activity α , showing the emergence of new data points obtained by varying the coefficient Γ_2 . The additional points reveal a shift in the critical activity where the transition in flow structure occurs, compared to the fixed-parameter case. (b) Velocity magnitude distribution for $\alpha = -3$, illustrating a transition from an unimodal Gaussian profile to a bimodal distribution as ϕ becomes positive, indicating the onset of local ordering. (c) Corresponding distribution for $\alpha = -8$, where the sign reversal in ϕ leads to a collapse of bimodality and a return to Gaussian statistics, signaling the loss of extended flow coherence.